FEASIBILITY STUDY FOR DOUBLE-FOCUSING MASS SPECTROGRAPH

Prepared for
National Aeronautics and Space Administration
Manned Spacecraft Center
Space Sciences Procurement Branch
Houston, Texas 77058
Attention: Mr. L. T. Schmiech/BG921(T-46)

Contract NAS9-7843

EOS Report 3039-Final   10 December 1968

ELECTRO-OPTICAL SYSTEMS, INC.
A XEROX COMPANY
PASADENA, CALIFORNIA 91107 • 213/351-2351

CONTENTS

CONTENTS (Contd)

SECTION 1

INTRODUCTION

Electro-Optical Systems, Inc. submits this final progress report in compliance with the requirements of the NASA Manned Spacecraft Center Contract NAS9-7843. This report completes the period of effort from 1 April to 1 September 1968.

The substance of the report is a comprehensive study to determine the optimal parameters for the design of an astronaut-operated Double-Focusing Mass/Charge Spectrograph which might be used for the measurements of solar wind mass/charge number composition. Specifically, parameters pertinent to the design of such an instrument were analyzed with regard to their various interdependencies for the purpose of establishing an overall design approaching the following primary set of operating criteria:

a.	Resolution	1000 to 5000
b.	Mass/charge range	2 to 10
c.	Angular spread	$\pm 10^{\circ}$
d.	Velocity deviation	± 0.20

It was determined that item c, the angular spread, is not feasibly consistent with the remaining criteria. Because of the singular importance of the angular spread, much of the data are presented with reference to this parameter.

Items a, b, and d are mutually consistent. However, energy deviation was found to be much more restricted than velocity deviation. Also considered was the following set of secondary criteria:

e.	Sensitivity	to be defined
f.	Light flux rejection	10^{-7} to 10^{-8}
g.	Dimensions	15 x 15 x 45 cm
h.	Weight	$<$ 20 pounds
i.	Power	10 to 20 watts

Sensitivity is discussed and defined in a manner which is convenient for the proposed use of the instrument.

Light flux rejection is an inherent feature of a tandem double-focusing instrument which is the design considered in this report. In addition, an innovation is described which would further enhance light rejection.

It has been conservatively estimated that the weight of the instrument and electronic components is less than 25 pounds.

It has been determined that the high voltage requirements, rather than power considerations, are more critical to the design concept which is presented.

SECTION 2

THEORETICAL CONSIDERATIONS

2.1 PROCEDURE

Transfer matrix methods for calculating trajectories are well known in optics and have been applied to electron optics. The application of these methods to electrostatic and magnetic deflectors has been gaining increasing recognition in recent years. Consequently, they are particularly adaptable to the study of double-focusing mass spectroscopic instruments. The transfer matrices used in this study were taken from References 1 through 5.

Essentially, the transfer matrix approach is a method of ray tracing. For example, in the case of ion optics an element (e.g., an electric or a magnetic sector) is represented by a transformation (transfer matrix) which gives description to an ion beam which has traversed the element. In order to effect such a description, the ion beam is represented by a vector, the components of which are formed by the entrance slit dimensions, entrance angular spread, and the deviations in mass/charge ratio and energy. The total transfer matrix which describes the path of an ion beam from entrance slit to photographic plate is the product of as many as 11 individual matrices. Among these are included the important effects of the fringe fields of both the electric and the magnetic sectors and the effect of changing the sense of the beam deflection.

After the total transfer matrix (one each for radial and axial deflections) has been obtained, then the mass/charge dispersion, the magnification, and the first and second order aberration coefficients can be identified. The axial aberrations are usually not considered past first order but the radial aberrations are calculated to second order and sometimes estimated to third order. In the present study, third order angle coefficients were included, and were assumed to have values 10 times that of the corresponding second order coefficients. The instrument resolution is calculated from elements of the total radial transfer matrix.

2.2 SIGNIFICANT ELEMENTS OF THE TOTAL RADIAL SECOND ORDER TRANSFER MATRIX

The total radial second order transfer matrix contains 289 elements of which only 17 are used in a determination of the resolving power of the instrument. These are given the notations as follows:

$$A_u,\ A_\alpha,\ A_\gamma,\ A_\delta,\ A_{uu},\ A_{u\alpha},\ A_{u\gamma},\ A_{u\delta},\ A_{\alpha\alpha},\ A_{\alpha\gamma},\ A_{\alpha\delta},\ A_{\gamma\gamma},\ A_{\gamma\delta},$$
$$A_{\delta\delta},\ A_{vv},\ A_{v\beta},\ A_{\beta\beta}$$

where α and β are the radial and axial half-angles, respectively. The quantities γ and δ are the mass/charge and energy deviations, respectively, defined as follows:

$$U = U_o[1 + \delta] \quad (1)$$
$$(M/Z) = (M/Z)_o[1 + \gamma] \quad (2)$$

where

U - particle energy per unit charge

U_o - particle energy per unit charge for central ray

(M/Z) - particle mass/charge number

$(M/Z)_o$ - particle mass/charge number with energy per unit charge U_o

The radial and axial displacements of the paraxial ray from the central ray are ur_m and vr_m where r_m is the radius of curvature of the central ray in the main magnetic field.

The most important of the 17 elements listed above are identified as follows:

A_u - magnification
A_α - first order radial angle aberration coefficient
A_δ - first order energy aberration coefficient
A_γ - mass dispersion coefficient
$A_{\alpha\alpha}$ - second order radial angle aberration coefficient
$A_{\alpha\delta}$ - second order radial angle-energy aberration coefficient
$A_{\delta\delta}$ - second order energy aberration coefficient
$A_{\beta\beta}$ - second order axial angle aberration coefficient

The third order coefficients of interest are:

$A_{\alpha\alpha\alpha}$ - third order radial angle aberration coefficient
$A_{\beta\beta\beta}$ - third order axial angle aberration coefficient

2.3 SIGNIFICANT ELEMENTS OF THE TOTAL AXIAL TRANSFER MATRIX

The axial transfer matrix first order elements are usually the only ones of interest and are denoted by:

A_v - magnification
A_β - first order axial angle aberration coefficient

2.4 INPUT PARAMETERS

The matrix elements are very lengthy, complicated functions of the input parameters. These parameters are given below:

φ_m	-	magnetic sector angle
φ_e	-	electric sector angle
D	-	(separation between the electric and magnetic sectors) x $1/r_m$
I'_α	-	parameter describing electric fringe field (input side)
I''_α	-	parameter describing electric fringe field (output side)
I'_β	-	parameter describing magnetic fringe field (input side)
I''_β	-	parameter describing magnetic fringe field (output side)
ϵ'	-	angle between the central ray and the normal to the input ideal field boundary of the magnetic sector
ϵ''	-	similar to ϵ' except refers to the output ideal field boundary of the magnetic sector
c	-	parameter describing the inhomogeneity of the main electric field
n	-	parameter describing the inhomogeneity of the main magnetic field
$\bar{Q}'$	-	[reciprocal radius of curvature of electric sector boundary (input side)] x r_m
$\bar{Q}''$	-	[reciprocal radius of curvature of electric sector boundary (output side)] x r_m
$\bar{R}'$	-	[reciprocal radius of curvature of magnetic sector boundary (input side)] x r_m
$\bar{R}''$	-	[reciprocal radius of curvature of magnetic sector boundary (output side)] x r_m
r_e	-	radius of curvature of central path in the main electric field
r_m	-	radius of curvature of central path in the main magnetic field
sense	-	determines the relative deflections in the electric and magnetic sectors

2.5 COMPUTER METHODS

A computer program was written to evaluate the radial and axial transfer matrices for the complete system. This merely required doing a series of matrix multiplications, each matrix being the transfer matrix for a given region (i.e., fringing field region, electric sector region, etc.). Due to the rather large dimensions of the radial matrices (17 x 17), the evaluation of the complete radial transfer matrix required about 23 seconds on the CDC-3100 computer. The first row of this radial matrix then determined the image slit width (for a given object slit) in terms of the 15 parameters describing the system: c, n, φ_e, φ_m, ϵ', ϵ'', I'_α, I''_α, r_e/r_m, D, $\overline{Q}'$, $\overline{Q}''$, $\overline{R}'$, $\overline{R}''$, and INVERT. The first row of the 2 x 2 first order complete axial transfer matrix rendered the image slit length. Several cases were run this way in a sort of trial and error approach to finding a good set of system parameters, and it also served as a means of checking out the program for possible coding errors. Once the program was debugged, it was changed into a subroutine to be used by yet another bigger program. The purpose of this new program was to try and find a combination of the input (system) parameters that would result in an improvement over a set of "initial guess" parameters. The program operated as follows: An "error" function, ERROR, was invented. It essentially indicated the radial aberration of the image slit due to particles of incident angle (α) and energy deviation energy (δ). Thus:

$$\text{ERROR}\,(c, n, \varphi_e, \varphi_m, \epsilon', \epsilon'', r_e/r_m, D, \overline{Q}', \overline{Q}'', \overline{R}', \overline{R}'', \text{INVERT}) = (2\alpha A_\alpha)^2 + (\alpha^2 A_{\alpha\alpha})^2 + (2\alpha\delta A_{\alpha\delta})^2 + (\delta^2 A_{\delta\delta})^2 + (2\delta A_\delta)^2$$

where the A's are the first row matrix elements of the complete radial transfer matrix. The values of α and δ were both arbitrarily set at 0.1.

The problem was now to minimize the ERROR function with respect to the various input parameters. (Actually, the parameters c, n, and INVERT were maintained at constant values and only the remaining 12 parameters were allowed to vary.) To find a minimum of a function, one merely computes the gradient of the function and then starts stepping backwards. This is exactly what was done. The 12 quantities:

$$\frac{\partial(\mathrm{ERROR})}{\partial\phi e}, \quad \frac{\partial(\mathrm{ERROR})}{\partial\phi m}, \quad \ldots, \quad \frac{\partial(\mathrm{ERROR})}{\partial\bar{R}''}$$

were calculated. Then, the components of the normalized gradient were computed:

$$\overline{(\nabla\ \mathrm{ERROR})_p} = \frac{\dfrac{\partial(\mathrm{ERROR})}{\partial p}}{\sqrt{\sum\limits_{k=1}^{12}\left[\dfrac{\partial(\mathrm{ERROR})}{\partial p_k}\right]^2}}, \quad p = \phi e, \phi m, \quad \ldots, \quad \bar{R}''.$$

An initial step size of 1.0 was chosen and this amount was "stepped off" in the direction of the negative gradient. (Note: this step was taken in 12-space, not on each parameter; consequently, each parameter changed by considerably less than 1.0 per step.) After each step the gradient was again re-computed to determine the direction in which the next step should be made. This process continued as long as the value of ERROR continued to decrease. Then, when a step in the direction of $-\nabla(\mathrm{ERROR})$ finally resulted in "going uphill", it was reasoned that a minimum had been overshot. So, the step size was reduced by a factor of 10 and the search continued at this smaller step size.

This above process was to continue until the step size became less than a certain value (about 0.001), at which point the minimum of the ERROR function would be claimed and the search would be over.

Unfortunately, things did not work completely according to plan. After the first "over-shooting" of the minimum with a step size of 1.0 it would seem plausible that by reducing the step size to 0.1 the minimum should be over-shot again within about ten steps at most. This never happened. Instead the step-off would continue in units of 0.1 well past the expected 10 iterations. It is difficult to say just how long this step size would continue to last since the time estimate of the program would always be exceeded, even when more than 1 1/2 hours was allowed. The main problem with the program was the amount of time it took. Since each evaluation of a gradient required an evaluation of the complete transformation matrix 12 times (one for each parameter), the time required for just one iteration step was almost 5 minutes! However, a later feature of the program allowed any of the parameters to be held fixed while the rest varied. This helped to increase the iteration frequency, although no minimum as such was ever found within the 99 minutes of time allotted per computer run.

2.6 RESOLUTION CLOSE TO THE CENTRAL RAY POINT AT THE IMAGE PLANE

Resolution (R), as described in Fig. 1, is defined as follows:

$$R = \frac{M/Z}{\Delta(M/Z)} \quad \text{or} \quad \frac{1}{2\gamma} \tag{3}$$

This is the resolution which can be obtained close to the central ray point of the image plane and is given analytically by the following expression:

$$R = \frac{0.5\, r_m A_\gamma}{S' A_u + r_m[2\alpha A_\alpha + 2\delta A_\delta + \alpha^2 A_{\alpha\alpha} + 2\alpha\delta A_{\alpha\delta} + \delta^2 A_{\delta\delta} + \beta^2 A_{\beta\beta} + 2\alpha^3 A_{\alpha\alpha\alpha} + 2\beta^3 A_{\beta\beta\beta}]} \tag{4}$$

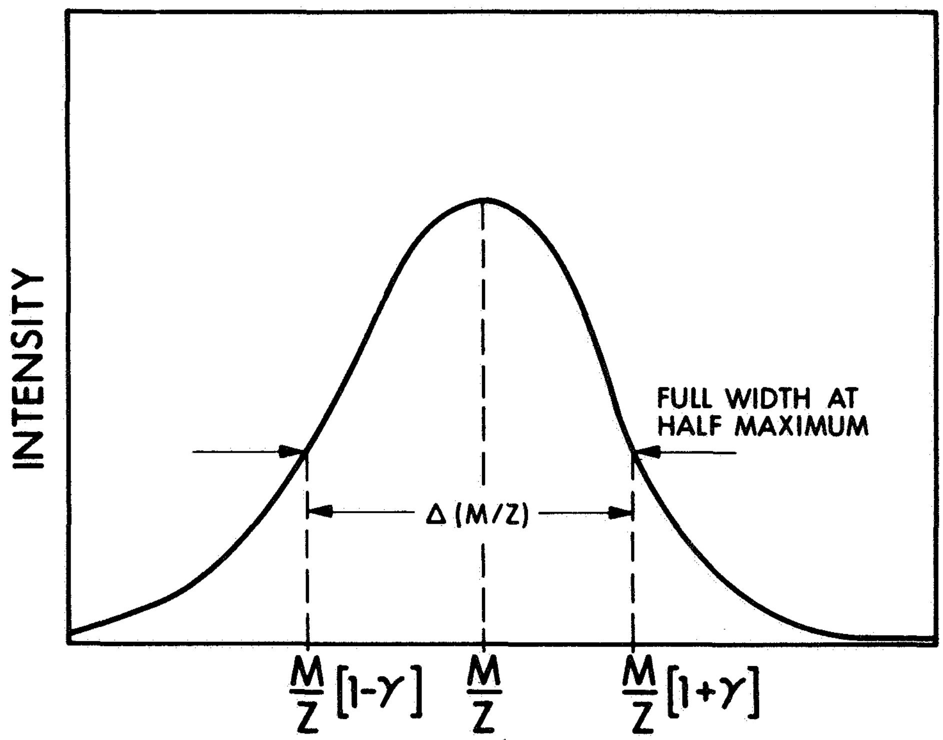

Figure 1. Definition of Resolution

where the values of all coefficients are taken as absolute. That is, minus signs are ignored. The S' ($=2u_o r_m$) is the width of the entrance slit (object). It should be noted that the length of the entrance slit is $2v_o r_m$.

Ideally, the best instrument design would be one for which all the aberration coefficients (except A_u and A_γ) vanished simultaneously. As can be seen in Eq. 4, it is desirable for A_γ to be as large as possible, and A_u to be minimized to less than unity.

2.7 DOUBLE-FOCUSING CONFIGURATIONS

The aberration coefficients for about 650 configurations were calculated. Most of these were slight modifications of a set of initial conditions on the parameters. In no case were the coefficients pertaining to α and δ made to assume insignificantly small values, simultaneously. During the study, values of the coefficients were observed to range from 10^{-5} to over 100.

Tables 1 through 4 contain the parameters and coefficients considered to be the best of the configurations studied. The data of Table 1 has been used in the selection of the design concept presented in this report. The notation scheme for this design is shown in Fig. 2.

TABLE 1

DOUBLE-FOCUSING MASS/CHARGE SPECTROGRAPH NO. 1

Dimensionless Physical Parameters

c =	1.00
n =	.91
ϕ_e =	70.95
ϕ_m =	120.45
ϵ' =	4.92
ϵ'' =	-61.99
I_α' =	-0.060
I_α'' =	.050
r_e/r_m =	.749
D =	.311
$\overline{Q}'$ =	0
$\overline{Q}''$ =	.010
$\overline{R}'$ =	-0.286
$\overline{R}''$ =	-0.010
L_e =	.294
L_m =	.441
Sense =	Opposite

Aberration Coefficients

A_u =	-.6531
A_α =	.000702
A_γ =	-.6157
A_δ =	.01434
A_{uu} =	.1837
$A_{u\alpha}$ =	-.5309
$A_{u\gamma}$ =	1.726
$A_{u\delta}$ =	2.098
$A_{\alpha\alpha}$ =	-1.258
$A_{\alpha\gamma}$ =	.564
$A_{\alpha\delta}$ =	-.01669
$A_{\gamma\gamma}$ =	1.226
$A_{\gamma\delta}$ =	.7263
$A_{\delta\delta}$ =	-.5409
A_{vv} =	1.368
$A_{v\beta}$ =	.3231
$A_{\beta\beta}$ =	-.2251
A_v =	-1.64
A_β =	-1.084

TABLE 2

DOUBLE-FOCUSING MASS/CHARGE SPECTROGRAPH NO. 2

Dimensionless Physical Parameters		Aberration Coefficients	
c =	1.25	A_u =	-.7416
n =	.90	A_α =	-.0002190
ϕ_e =	65.36	A_γ =	-.9023
ϕ_m =	101.84	A_δ =	.03507
ϵ' =	4.17	A_{uu} =	-.8761
ϵ'' =	-42.54	$A_{u\alpha}$ =	-1.783
I_α' =	-0.02	$A_{u\gamma}$ =	-.005096
I_α'' =	.05	$A_{u\delta}$ =	2.765
r_e/r_m =	.809	$A_{\alpha\alpha}$ =	-3.229
D =	.486	$A_{\alpha\gamma}$ =	1.391
$\bar{Q}'$ =	0	$A_{\alpha\delta}$ =	.03657
$\bar{Q}''$ =	-0.01	$A_{\gamma\gamma}$ =	.6379
$\bar{R}'$ =	.02	$A_{\gamma\delta}$ =	1.721
$\bar{R}''$ =	-0.09	$A_{\delta\delta}$ =	-.8268
L_e =	.679	A_{vv} =	1.268
L_m =	.973	$A_{v\beta}$ =	2.308
Sense =	Opposite	$A_{\beta\beta}$ =	1.034
		A_v =	-1.777
		A_β =	-1.961

TABLE 3

DOUBLE-FOCUSING MASS/CHARGE SPECTROGRAPH NO. 3

Dimensionless Physical Parameters		Aberration Coefficients	
c =	1.00	A_u =	-.8297
n =	.90	A_α =	.001298
ϕ_e =	68.76	A_γ =	-.7880
ϕ_m =	111.98	A_δ =	.01404
ϵ' =	-1.96	A_{uu} =	-1.133
ϵ'' =	-50.46	$A_{u\alpha}$ =	-.6416
I_α' =	-0.060	$A_{u\gamma}$ =	-.1032
I_α'' =	.050	$A_{u\delta}$ =	3.102
r_e/r_m =	.773	$A_{\alpha\alpha}$ =	-1.800
D =	.393	$A_{\alpha\gamma}$ =	1.061
$\bar{Q}'$ =	0	$A_{\alpha\delta}$ =	.007463
$\bar{Q}'$ =	.010	$A_{\gamma\gamma}$ =	.656
$\bar{R}'$ =	.050	$A_{\gamma\delta}$ =	1.611
$\bar{R}''$ =	-0.010	$A_{\delta\delta}$ =	-.5644
L_e =	.337	A_{vv} =	1.123
L_m =	.670	$A_{v\beta}$ =	.7686
Sense =	Opposite	$A_{\beta\beta}$ =	.2305
		A_v =	-1.608
		A_β =	-1.114

TABLE 4

DOUBLE-FOCUSING MASS/CHARGE SPECTROGRAPH NO. 4

Dimensionless Physical Parameters		Aberration Coefficients	
c =	1.00	A_u =	-1.054
n =	.90	A_α =	-.004138
ϕ_e =	65.59	A_γ =	-1.004
ϕ_m =	97.70	A_δ =	.02480
ϵ' =	4.07	A_{uu} =	-1.736
ϵ'' =	-37.90	$A_{u\alpha}$ =	-1.218
I_α' =	-0.07	$A_{u\gamma}$ =	-.5994
I_α'' =	.05	$A_{u\delta}$ =	3.910
r_e/r_m =	.838	$A_{\alpha\alpha}$ =	-2.633
D =	.506	$A_{\alpha\gamma}$ =	1.317
$\bar{Q}'$ =	0	$A_{\alpha\delta}$ =	.003562
$\bar{Q}''$ =	.01	$A_{\gamma\gamma}$ =	.6275
$\bar{R}'$ =	.05	$A_{\gamma\delta}$ =	2.028
$\bar{R}''$ =	-0.01	$A_{\delta\delta}$ =	-.7918
L_e =	.414	A_{vv} =	1.006
L_m =	1.133	$A_{v\beta}$ =	1.311
Sense =	Opposite	$A_{\beta\beta}$ =	.4963
		A_v =	-1.753
		A_β =	-1.410

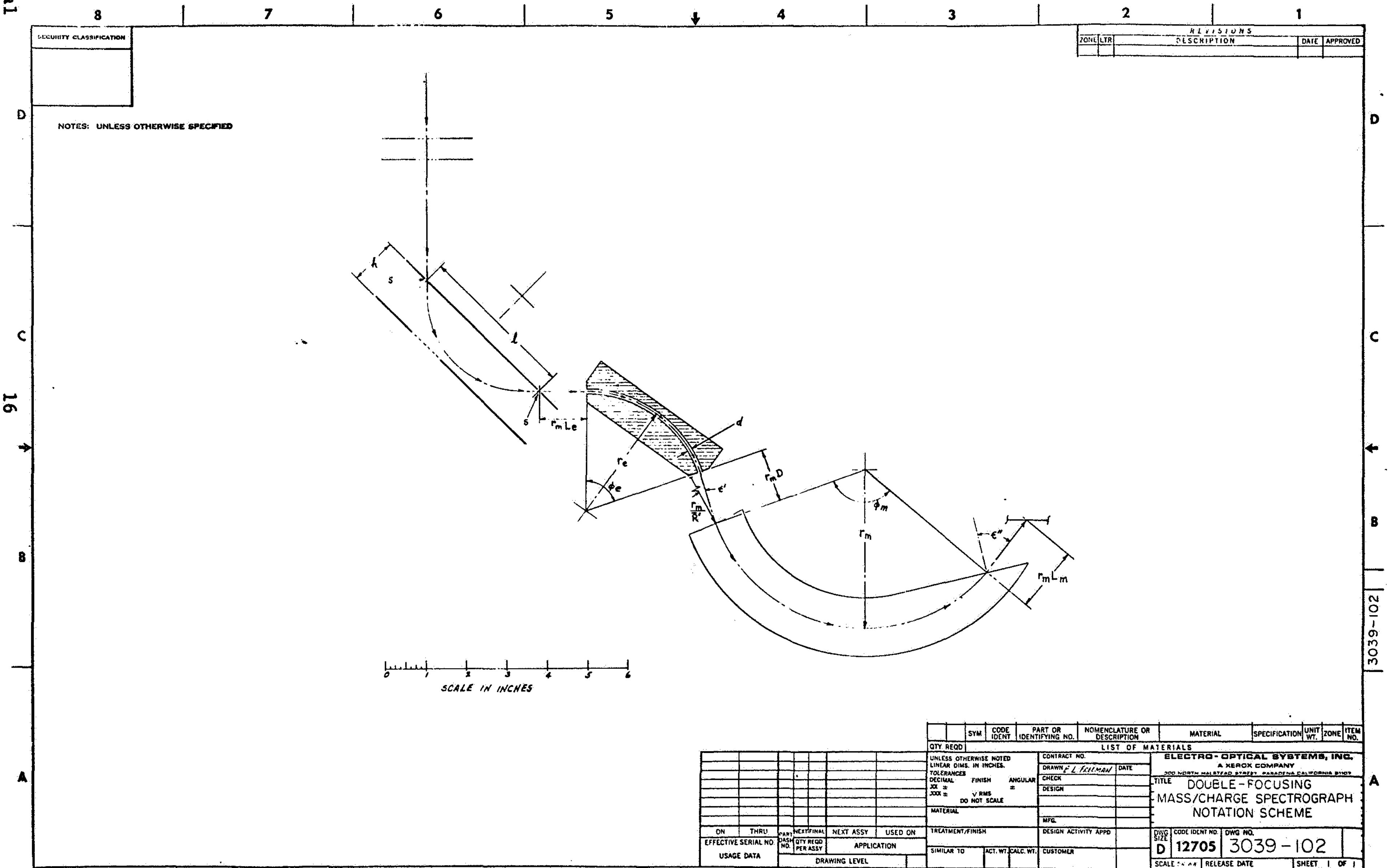
NOTES: UNLESS OTHERWISE SPECIFIED
SECURITY CLASSIFICATION
REVISIONS
ZONE LTR DESCRIPTION DATE APPROVED
h
s
l
s
$r_m L_e$
r_e
ϕ_e
d
ϵ'
$r_m D$
$\frac{r_m}{R'}$
ϕ_m
r_m
ϵ''
$r_m L_m$
SCALE IN INCHES
0 1 2 3 4 5 6
LIST OF MATERIALS
ELECTRO-OPTICAL SYSTEMS, INC.
A XEROX COMPANY
TITLE DOUBLE-FOCUSING MASS/CHARGE SPECTROGRAPH NOTATION SCHEME
DWG SIZE D
CODE IDENT NO. 12705
DWG NO. 3039-102
SHEET 1 OF 1
3039-102

Figure 2.

SECTION 3

DESIGN CONSIDERATIONS

3.1 ENERGY DISPERSION AND DEVIATION

Image aberrations in the spectrograph can be reduced by the proper choice of design parameters, as previously discussed, and also by decreasing the direction angles, α and β, and the energy deviation, δ. The direction angles can be controlled with comparative ease by collimating the beam, using a proper slit arrangement. However, decreasing the energy deviation requires a technique which disperses the beam in such a way that only particles with energies within the deviation can filter through. A simple device, the parallel-plate electric field mirror, accomplishes this purpose. Only particles entering the mirror with energy/charge within a given deviation, δ, are able to pass through and into the electric sector of the spectrograph, the direction angles remaining unchanged. Figure 3 presents a design concept showing the mirror arrangement which has been identified as the energy filter.

3.1.1 THE MIRROR ANALYZER AND CALCULATION OF δ

The theory of the mirror is simple when compared with other geometries of electrostatic analyzers[6]. The ion paths are parabolic with the slits, S, located to pass those particles with energy, U_o, which enter and leave at an angle of 45^o with respect to the normal or those particles with an energy, $U > U_o$, which enter and leave at an angle, $\pm\alpha$, with respect to the 45^o direction. The mean distance, ℓ (see Figure 2), between the entrance and exit slits is given by

$$\ell = \frac{2U_o h}{V_F} [1 + \delta] \cos 2\alpha \qquad (5)$$

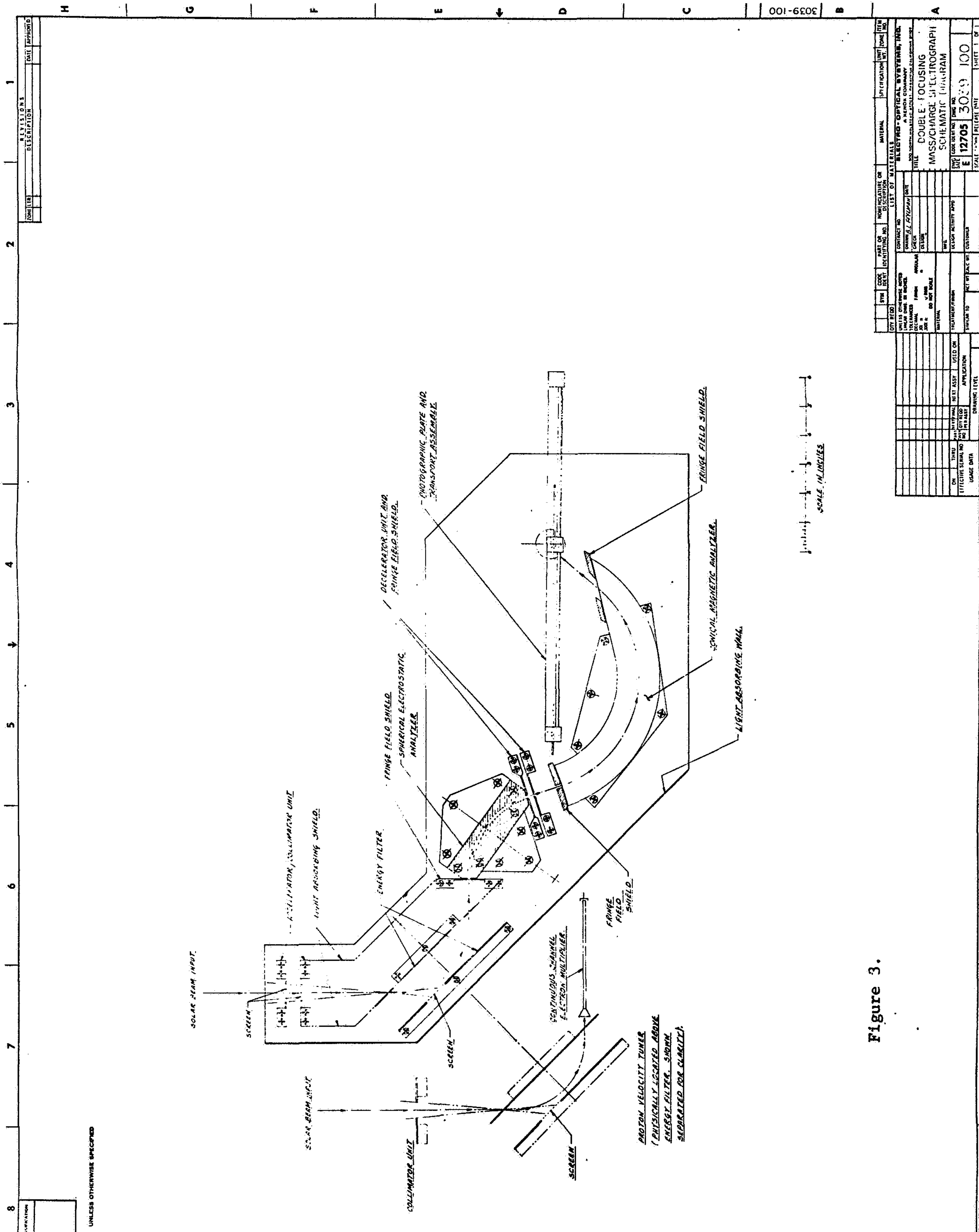
3039-100
SOLAR BEAM INPUT
SCREEN
ACCELERATOR, COLLIMATOR UNIT
LIGHT ABSORBING SHIELD
ENERGY FILTER
FRINGE FIELD SHIELD
SPHERICAL ELECTROSTATIC ANALYZER
DECELERATOR UNIT AND FRINGE FIELD SHIELD
PHOTOGRAPHIC PLATE AND TRANSPORT ASSEMBLY
FRINGE FIELD SHIELD
CONICAL MAGNETIC ANALYZER
LIGHT ABSORBING WALL
SCALE IN INCHES
FRINGE FIELD SHIELD
CONTINUOUS CHANNEL ELECTRON MULTIPLIER
SCREEN
PROTON VELOCITY TUNER (PHYSICALLY LOCATED ABOVE ENERGY FILTER, SHOWN SEPARATED FOR CLARITY)
SOLAR BEAM INPUT
COLLIMATOR UNIT
SCREEN
NOTES: UNLESS OTHERWISE SPECIFIED
LIST OF MATERIALS
ELECTRO-OPTICAL SYSTEMS, INC.
DOUBLE-FOCUSING MASS/CHARGE SPECTROGRAPH SCHEMATIC DIAGRAM
E 12705 3039 100

Figure 3.

where V_F is the potential across the mirror plates. This potential can be evaluated in terms of U_o by letting $\alpha = 0$ in which case $\delta = S/\ell$, as will be shown. Therefore,

$$V_F = \frac{2U_o h[1 + S/\ell]}{\ell} \qquad (6)$$

For the usual case, $S \ll \ell$, the term in the parentheses is of little importance.

Referring to the dimensions given in Figure 2, i.e., ℓ = 100 mm (3.937") h = 2.921 mm (1.150") renders $V_F = 0.584U_o$.

Equation 5 can be used to determine δ by considering the illumination of the exit slit, as follows:

Ion beam enters mirror at $\alpha = 0$;

illumination = full - $U = U_o$

illumination $\rightarrow$ 0 - $U \rightarrow U_o[1 \pm S/\ell] = U_o[1 + \delta]$

Ion beam enters mirror at $\alpha \neq 0$;

illumination = full - $U = U_o \sec 2\alpha = U_o[1 + \delta]$

illumination $\rightarrow$ 0 - $U \rightarrow U_o[1 \pm S/\ell]\sec 2\alpha = U_o[1 + \delta]$

Therefore, the maximum deviation, $\delta(\max)$, occurs when $\alpha \neq 0$, i.e.,

$$\delta(\max) = [1 + S/\ell]\sec 2\alpha - 1$$

and, the minimum deviation, $\delta(\min)$, occurs when $\alpha = 0$, i.e.,

$$\delta(\min) = -S/\ell$$

The range of deviation that can be transmitted through the exit slit is then given by

$$\begin{aligned}\delta(\max) - \delta(\min) &= [1 + S/\ell]\sec 2\alpha - 1 + S/\ell \\ &= 2\sec 2\alpha[\sin^2\alpha + (S/\ell)\cos^2\alpha] \\ &\approx 2[\alpha^2 + S/\ell] \text{ (for } \alpha < 10^\circ\text{)}\end{aligned}$$

Finally, δ is defined as one-half the range of deviation or

$$\delta = \alpha^2 + S/\ell \tag{7}$$

Equation 7 shows the dependence of the energy deviation on the radial acceptance half-angle, which is peculiar to the design concept presented in Figure 3.

3.1.2 THE MIRROR ANALYZER AND VELOCITY TUNING

Figure 3 also shows a separate parallel-plate mirror, the proton velocity tuner, which is physically mounted on top of the energy filter and is in every respect identical to the latter. This unit is tuned to an energy such that the maximum proton current is delivered to a continuous channel electron multiplier. In this manner it is possible to monitor changes of the proton bulk velocity, V_o, and hence of the other ionic species in the solar wind.

3.2 VELOCITY DEVIATION

It should be noted that decreasing the energy deviation, δ, does not require a decrease in the velocity deviation. On the contrary, a wide velocity deviation or random velocity distribution is desirable to the function of a double-focusing mass/charge spectrograph in its application to solar wind measurements. This is quite different from the electrostatic energy analyzer from which the best data resolution is obtained when the solar wind temperatures are low, i.e., when the random velocity distributions are relatively narrow. It would follow that high solar wind temperatures represent the best conditions for spectrograph operation. The reason for this is that particles with a deviation in mass/charge and a sufficiently large magnitude of velocity deviation, such that their energies have at most a deviation δ, will pass simultaneously through the spectrograph and, thus, be recorded on the photographic plate. The relation satisfying this condition is given in first order by

$$\text{VELOCITY DEVIATION} = \frac{\delta - \gamma}{2} \tag{8}$$

Equation 8 results from the fact that it is generally agreed among investigators of solar wind phenomena that all ion species have essentially the same bulk velocity, V_o. On the other hand, if it were assumed that all ion species had essentially the same temperature, then they could not have the same maxwellian velocity distributions. In particular, the heavier species would have extremely narrow distributions relative to those of the lighter ions. Thus, it would be inherently difficult to operate a spectrograph to measure mass/charge numbers for heavy ions. However, for a solar wind in the normal temperature range, $> 3 \times 10^4$ °K, there is a tendency for $^1H^+$ and $^4He^{++}$ random velocity distributions to have similar widths, implying $^4He^{++}$ temperatures ~ 4 times the $^1H^+$ temperatures.[7,8] Now, according to S. J. Bame, et al,[9] there are clear indications in the Vela data that the various ion species have more nearly equal temperatures when the solar wind is cold ($\sim 10^4$ °K). Therefore, normal-temperature solar wind has presumably undergone extensive non-thermal heating in interplanetary space, the heating processes tending to cause <u>different ion species</u> to have <u>nearly the same</u> random velocity distributions. It should be noted that during the 104 days of Mariner II data collection, ninety percent of the recorded temperatures were between 6×10^4 and 5×10^5 °K, i.e., normal to greater than normal.

In summary, it is necessary to have δ small for resolution and the velocity deviation at least large enough to obtain the desired range in mass/charge displayed simultaneously on the photographic plate. Again, from Mariner II data,[10] it was found that the proton velocity deviation was > 0.18 over several runs which had values of bulk velocity, V_o, extending from 315 to 840 km/sec. If, according to the above discussion, this value of velocity deviation can be applied to heavier ion species as well, then the requirements for the mass/charge ranges of interest will be satisfied regardless of the ion mass.

3.3 MASS/CHARGE COMPOSITION OF THE SOLAR WIND

The results of several solar wind experiments have positively identified the presence of mass/charge numbers one and two. The former is the proton content, of course, and the latter is considered to be alpha content. Data from the Vela 3A experiment[9] purports to show that $^{3}He^{++}$, $^{4}He^{+}$, various ion species of ^{16}O, and other unidentified heavy ions are present in the solar wind. J. Zirker[11] of the University of Hawaii has been investigating the existence of Fe^{+14}.

Table 5 was generated in order to relate various ion species in terms of mass/charge number. Elements helium to iron have been included with the range of mass/charge number extending from two to ten, correlating with all possible degrees of ionization occurring in that range. The table is incomplete to the extent that it does not contain isotopes of the elements. However, it furnishes a basis for determining the resolution requirements of an instrument designed to measure mass/charge. For example, referring to Figure 1 and Equation 3, a resolution of 143 would be required to distinguish $^{4}He^{+}$ (4.003) and $^{56}Fe^{+14}$ (3.989). On the other hand, a resolution of 3333 is necessary to resolve $^{4}He^{++}$ (2.0015) and $^{12}C^{+6}$ (2.0018).

TABLE 5

VARIOUS ION SPECIES IN TERMS OF MASS/CHARGE NUMBER

Atomic number	Element	Mass number																																										
2.	(He)	4.003	2.0015																				4.003																					
3.	(Li)	6.940				2.313											3.470																											
4.	(Be)	9.013			2.253								3.0044															4.507																
5.	(B)	10.82		2.164						2.705									3.607																		5.410							
6.	(C)	12.011	2.0018				2.402						3.0027										4.0036																				6.006	
7.	(N)	14.008	2.0011			2.335					2.802							3.502												4.669														
8.	(O)	16.000	2.000		2.286				2.667						3.200								4.000													5.333								
9.	(F)	19.00		2.111		2.375				2.714				3.167							3.800										4.750													
10.	(Ne)	20.183	2.018		2.243			2.523			2.883					3.364							4.037										5.046											
11.	(Na)	22.991	2.090		2.299			2.555			2.874				3.284						3.833								4.598											5.748				
12.	(Mg)	24.32	2.027		2.211		2.432			2.702			3.040				3.474						4.053								4.864												6.080	
13.	(Al)	26.98	2.075		2.248		2.453		2.498			2.998				3.373					3.854						4.497									5.396								
14.	(Si)	28.09	2.006	2.161		2.341		2.554			2.809			3.121				3.511					4.013							4.682									5.618					
15.	(P)	30.975	2.065		2.213	2.383		2.581			2.816		3.098				3.442				3.872						4.425							5.163										6.195
16.	(S)	32.066	2.0041	2.138	2.290		2.467		2.672			2.915			3.207			3.563					4.008					4.581								5.344								
17.	(Cl)	35.457	2.086		2.216	2.364		2.533		2.727		2.955			3.223			3.546				3.940					4.432						5.065									5.910		
18.	(A)	39.944			2.219	2.350	2.497		2.663		2.853		3.073			3.329			3.631			3.994					4.438					4.993								5.706				
19.	(K)	39.100	2.058	2.172		2.300	2.444		2.607	2.793			3.008		3.258			3.555				3.910				4.344					4.888							5.586						
20.	(Ca)	40.08	2.004	2.109	2.227	2.358		2.505	2.672		2.863		3.083			3.340			3.644				4.008				4.453						5.010							5.726				
21.	(Sc)	44.96		2.141	2.248	2.366	2.498		2.645		2.810	2.997			3.211		3.458			3.747			4.087				4.496					4.996							5.620					
22.	(Ti)	47.90		2.177	2.281	2.395		2.521	2.661		2.818	2.994		3.193			3.421		3.685			3.992				4.355				4.790						5.322						5.988		
23.	(V)	50.95			2.215	2.316	2.426	2.548	2.682		2.831	2.997		3.184		3.397			3.639			3.919			4.246				4.632				5.095						5.661					
24.	(Cr)	52.01		2.167	2.261	2.364	2.477		2.601	2.737	2.889		3.059		3.251		3.467			3.715			4.001			4.334				4.728					5.201					5.779				
25.	(Mn)	54.94		2.198	2.289	2.389	2.497		2.616	2.747	2.892		3.052		3.232		3.434		3.663			3.924			4.226			4.578				4.995					5.494							6.104
26.	(Fe)	55.85		2.148	2.232	2.327	2.428	2.539	2.660	2.793		2.939		3.103	3.285		3.491			3.723		3.989			4.296				4.654				5.077					5.585						

Part I

Part 2

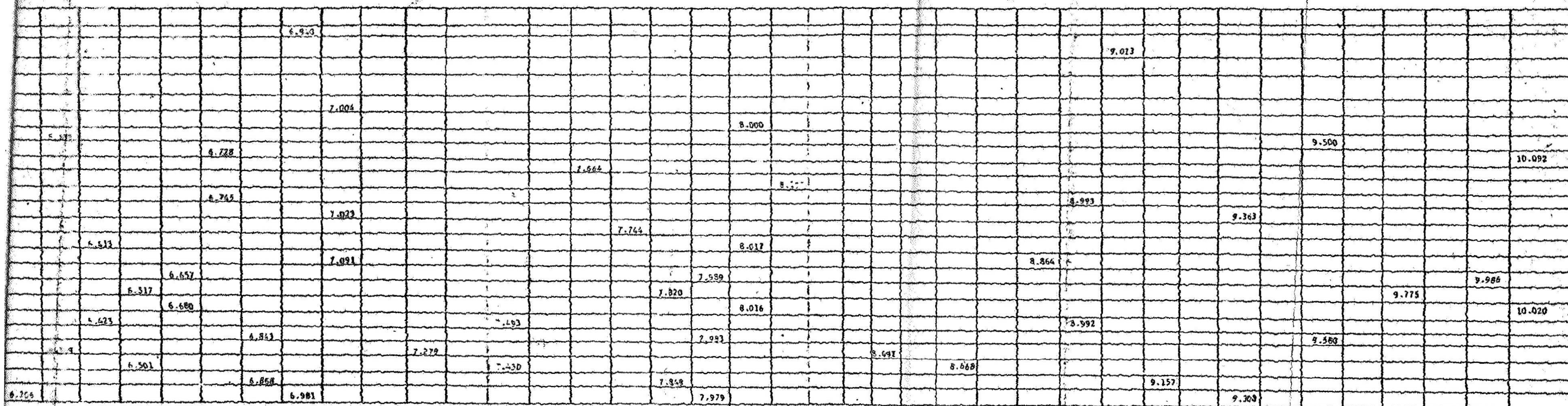
6.940
7.004
8.000
9.013
9.500
10.092
6.728
7.664
6.745
7.023
8.993
9.363
7.744
8.017
7.091
8.864
6.657
7.939
9.986
6.317
7.820
9.775
6.680
8.016
10.020
8.992
6.863
7.993
9.580
7.279
8.698
8.668
6.501
7.430
6.858
7.949
9.157
6.981
7.979
9.308

Figure 4 is a plot of the number of occurrences of a given mass/charge number in Table 5. Figure 5, an integration of Figure 4, shows that three-fourths of the total number of values of mass/charge numbers listed in Table 5 occur for $M/Z < 5$.

3.4 MEASUREMENT OF MASS/CHARGE (RANGE SELECTION)

In the common application of a mass spectrograph, the particles are generated within the instrument from an ion source. Consequently, the selection of particles within a given range of mass/charge number is accomplished by "tuning" the particle energy and electric sector voltage, simultaneously. In the present application the ion source is the solar wind. Normally, therefore, the selection would necessitate varying the magnetic field intensity as well as the electric sector voltage.

In order to avoid changing the magnetic field, thus permitting the use of one permanent magnet, a short retarding electric field (the decelerator unit of Figure 3), situated between the electric and magnetic sectors, is introduced into the design concept. The purpose of this field is to vary the energy of a particle as it enters the magnetic sector such that the product of the mass/charge times the energy equals a constant k. That is, since the magnetic intensity B is given by,

$$B = \frac{4470}{r_m} \sqrt{(M/Z)W} \quad \text{(gauss)} \tag{9}$$

where, W is the energy in kilovolts with which a particle with mass/charge number M/Z enters the magnetic sector, then,

$$(M/Z)W = k \tag{10}$$

A value of $k = 22.5$ has been chosen. This requires a magnetic field intensity $B = 2120$ gauss ($r_m = 10$ cm).

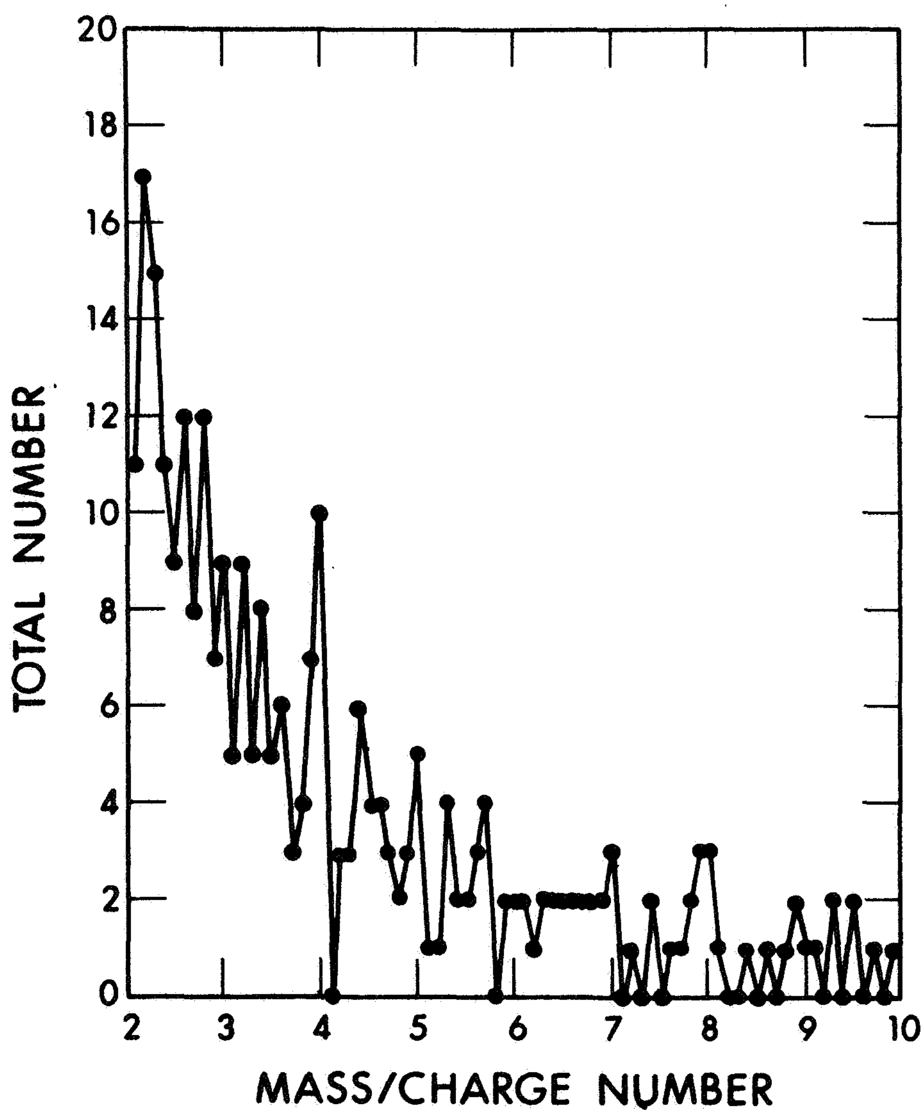

Figure 4. Number of Occurrences of Given Mass/ Charge-Number

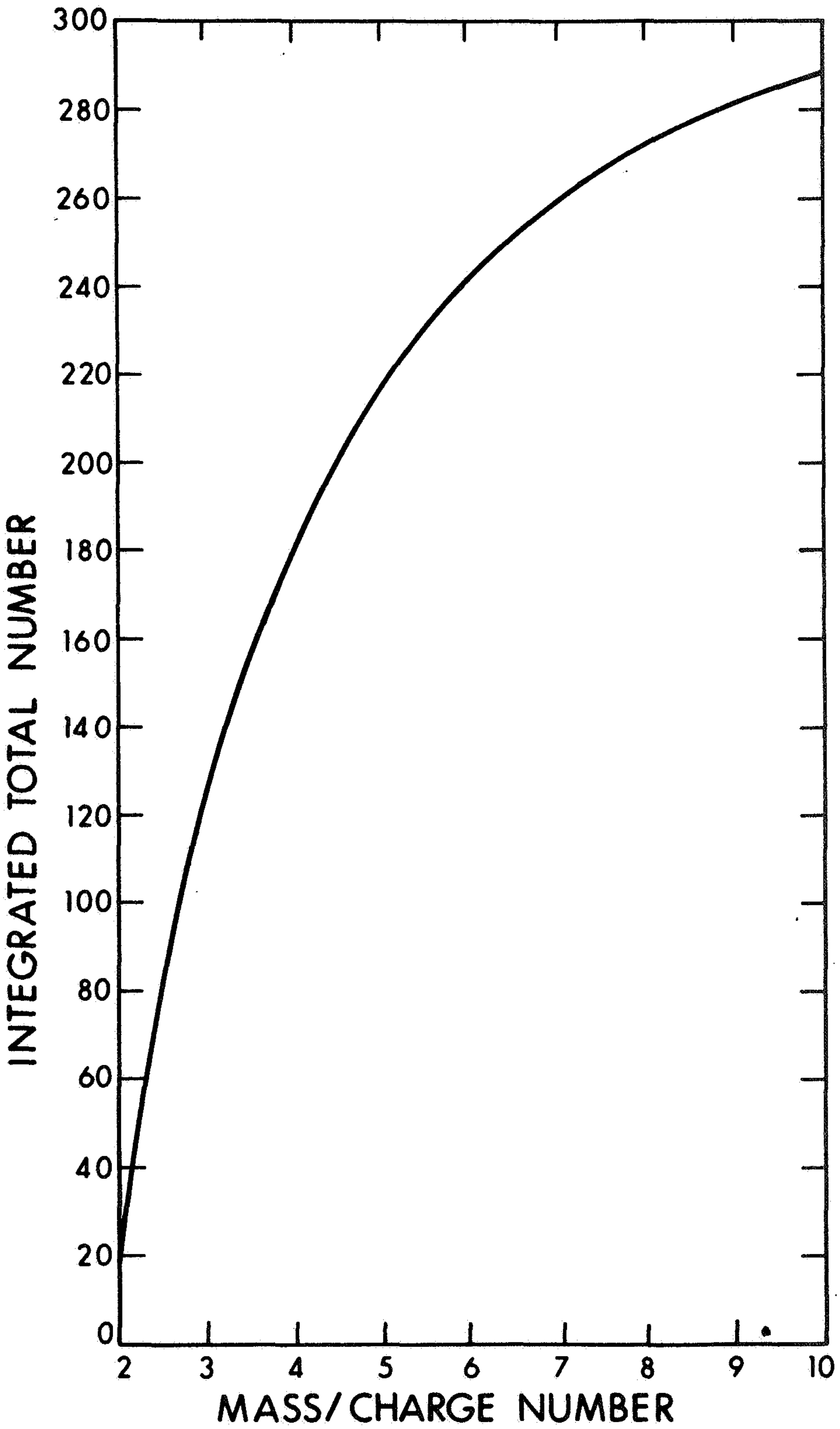

Figure 5. Integration of Mass/Charge Numbers

The ion beam incident into the decelerator unit must be highly collimated so that the retarding field does not cause angle dispersion. This is precisely the function of the spherical electrostatic analyzer. That is, this sector collimates a beam which is incident with angles α, β, and for which the energy deviation is small.

The accelerator unit which precedes the energy filter has two functions, one of which is to help satisfy the condition that $k = 22.5$ for $M/Z < 5$. The other function will be discussed in Subsection 3.5.

In effect, Table 6 explains the relative roles of the accelerator and decelerator units. In particular, it should be noted that the design concept permits the full range of the solar wind bulk velocity (300 to 700 km/sec) to be accepted by the instrument only for mass/charge numbers two through six. The "velocity window" becomes more restricted for the numbers seven through ten.

3.5 VIRTUAL ACCEPTANCE ANGLES VERSUS REAL ACCEPTANCE ANGLES

The real acceptance angles, α and β, are those which are seen by the instrument, beginning with the energy filter. The so-called virtual acceptance angles, α' and β', are those which are seen by the accelerator/collimator unit. In addition to its function in selecting mass/charge range from $M/Z < 5$, <u>this unit also effects a reduction (to α, β) of the angles α' and β'</u>. This feature is of primary importance because it causes an increase in the resolution for the lower mass/charge numbers and for a given α', β', over that which would result if the accelerator/collimator unit were not present.

The relationship between the two sets of angles can be shown to behave according to

TABLE 6

SCHEME FOR SELECTING MASS/CHARGE NUMBER

k = 22.5

$\frac{M}{Z}$	Approximate Accelerator Voltage (kV)	Approximate Decelerator Voltage Tuning Range (kV)	Acceptance Solar Wind Energy Range (kV)	Acceptance Solar Wind Bulk Velocity Range (km/sec)
2	10	0 to 4	0.9 to 5	300 to 700
3*	10*	4* to 10*	1.4* to 7.5*	300 to 700
4	6	2 to 10	1.8 to 10	300 to 700
5	2	0 to 10	2.3 to 12.5	300 to 700
6	1	0 to 11	2.7 to 14	300 to 700
7	0	0 to 10	3.2 to 13.2	300 to 610
8	0	1 to 10	3.6 to 12.8	300 to 570
9	0	1.5 to 10	4.1 to 12.5	300 to 530
10	0	2 to 10	4.5 to 12.3	300 to 480

* For example: $3[10 - 4 + 1.4] \approx 3[10 - 10 + 7.5] \approx k$

$$\frac{\alpha}{\alpha'} = \frac{\beta}{\beta'} = \sqrt{\frac{U_o}{U_o + V_{acc.}}} \tag{11}$$

where, $V_{acc.}$ is the potential across the accelerator unit. Figure 6 provides a plot of Equation 11 as a function of mass/charge numbers for the full range of solar wind bulk velocity. As can be seen in the figure, the fractional angle reduction will depend upon the velocity for numbers less than seven. However, for $M/Z > 7$ no reduction can be expected because of the selected values of magnetic field intensity and maximum accelerator voltage.

Equations 7 and 11 were used to calculate the plot of Figure 7 which is the maximum energy deviation corresponding to that curve of Figure 6 which pertains to the upper limit of velocity.

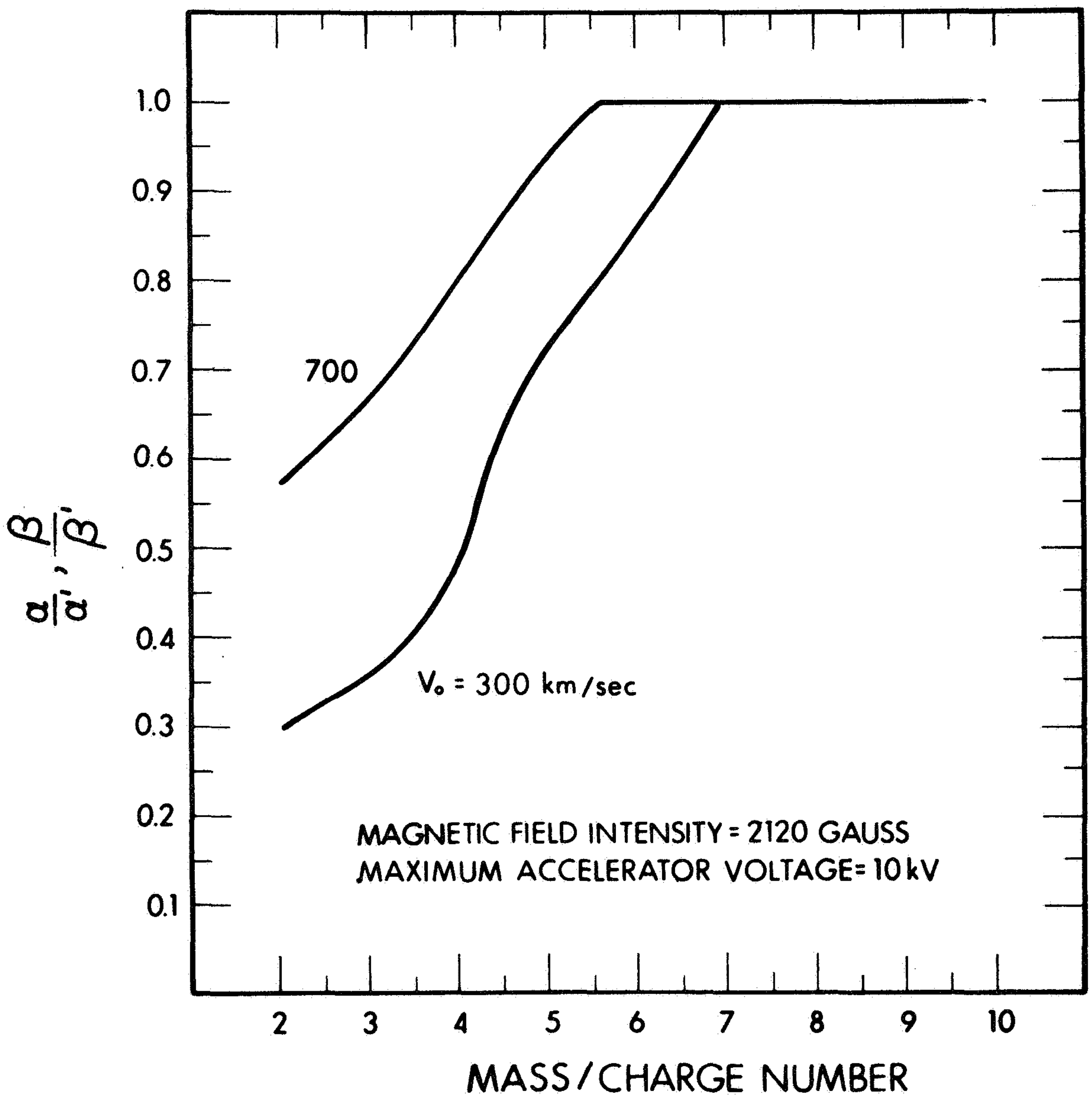

Figure 6. Equation 11 as a Function of Mass/Charge Numbers for the Full Range of Solar Wind Bulk Velocity

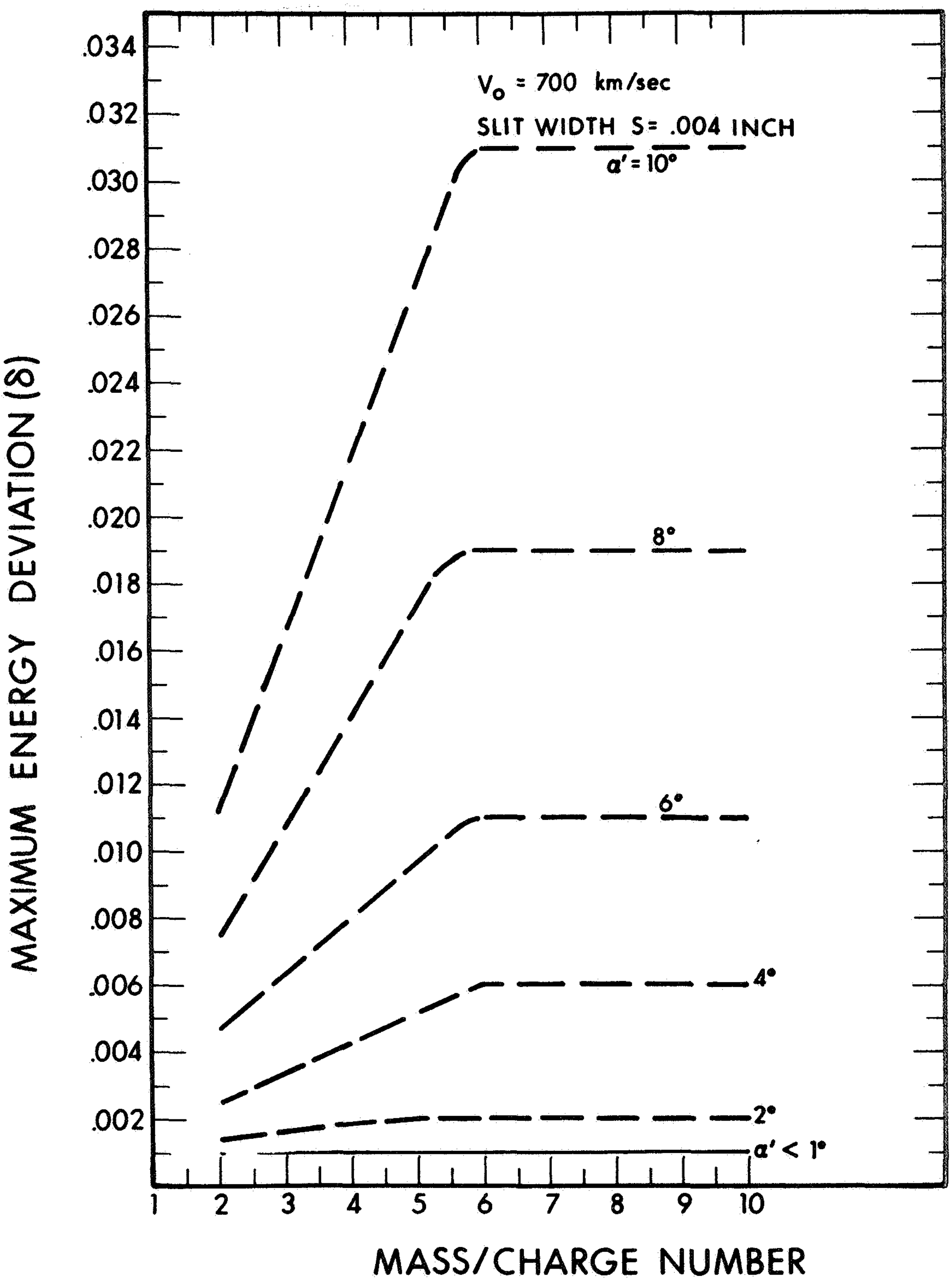

Figure 7. Maximum Energy Deviation Pertaining to the Upper Limit of Velocity

3.6 CALCULATION OF RESOLUTION

It is now possible to calculate resolution using Eq. 4. Values of r_m, and the first and second order aberration coefficients can be obtained from Table 1. The third order coefficients in α and β are assumed to be one order of magnitude greater than their second order counterparts (Ref. 12). Cross third order terms between α and δ have been neglected.

It should be noted (see Fig. 2) that the object slit, S, forms an angle 45° with the central path whereas the S' appearing in Eq. 4 refers to the width of a slit that is normal to the central path direction. Therefore,

$$S' = \frac{\text{OBJECT SLIT WIDTH}}{\sqrt{2}} \tag{12}$$

The energy deviation, δ, and the real acceptance half-angles, α and β, can be expressed from Eqs. 7 and 11, respectively, as functions of the virtual acceptance half-angles α' and β', which were defined in Section 3.5.

In order to simplify the presentation, the minimum resolution has been calculated. This minimum resolution corresponds to the upper limit of solar wind velocity, $V_o = 700$ km/sec. Plots of minimum resolution versus the virtual acceptance half-angle, α', are presented in Figs. 8, 9, and 10 for three widths of the object slit, S. Note that the curves for all mass/charge numbers would coincide with that labeled mass/charge = 6 to 10 if the accelerator/collimator unit were not used to accomplish angle reduction.

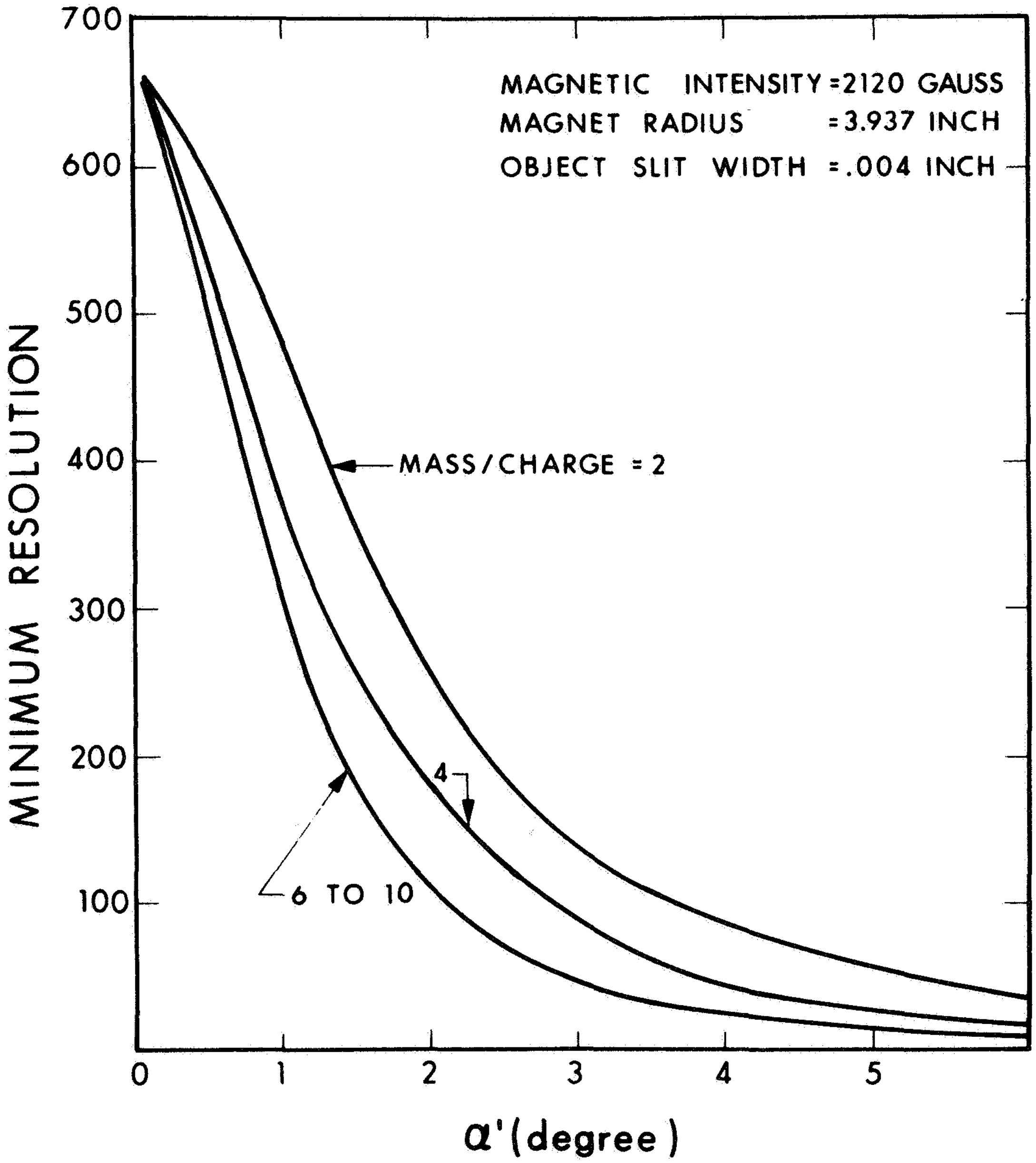

Figure 8. Spectrograph No. 1, Minimum Resolution versus Virtual Acceptance Half-Angle

31966

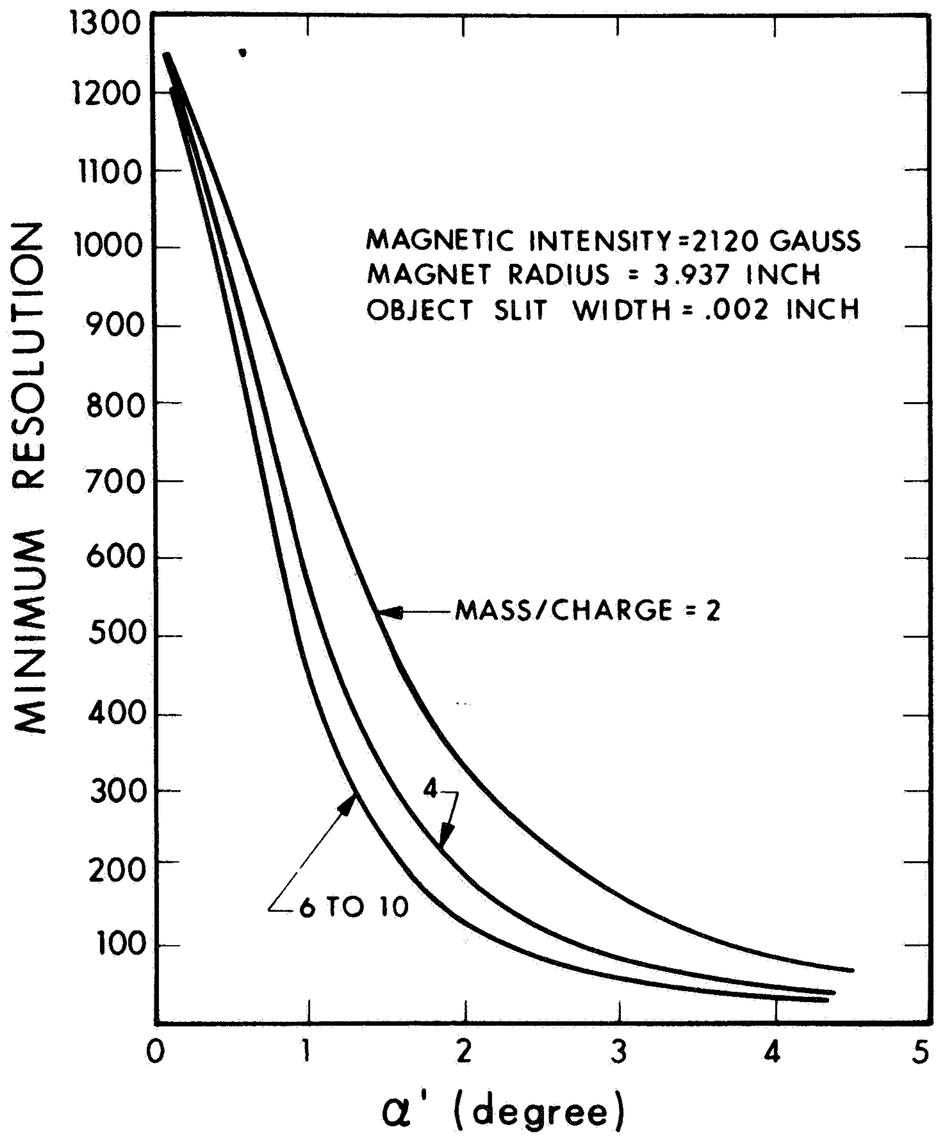

Figure 9. Spectrograph No. 1, Minimum Resolution versus Virtual Acceptance Half-Angle

31965

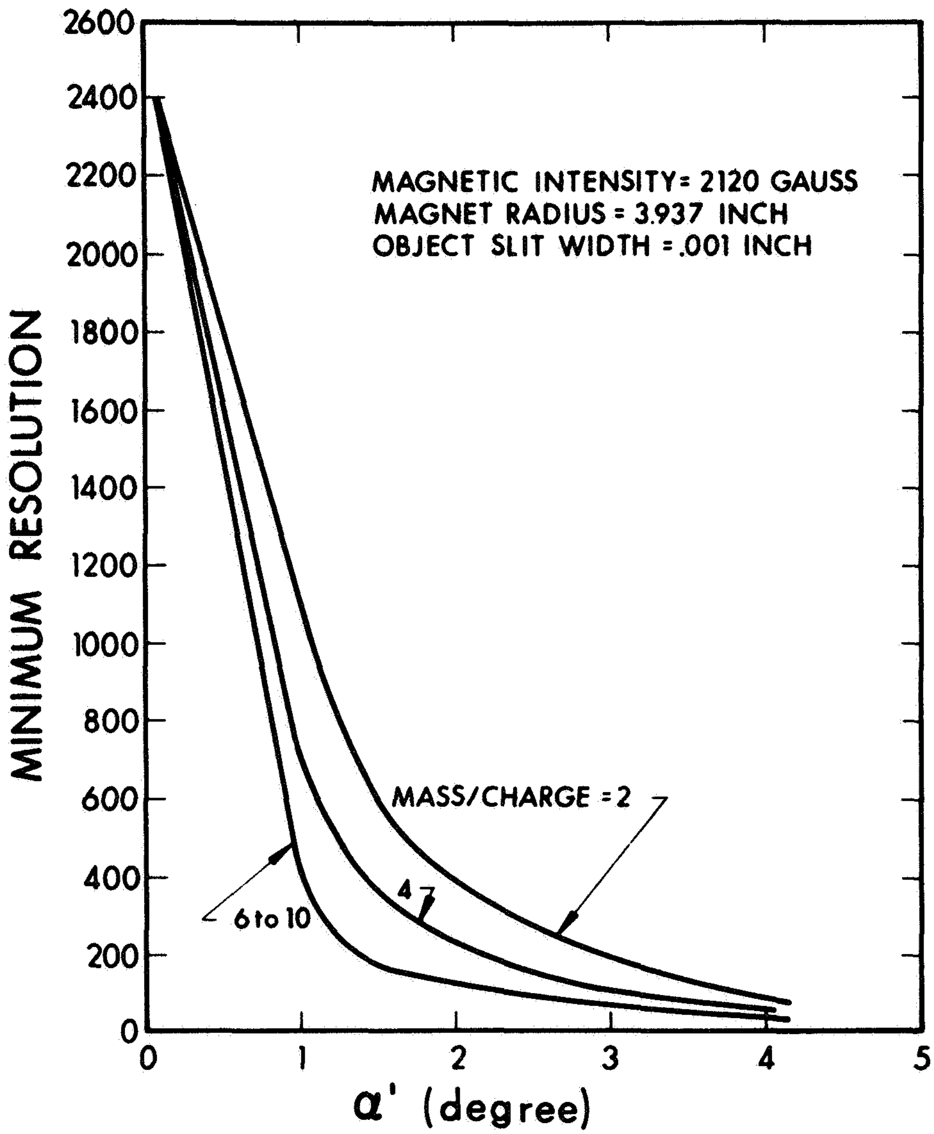

Figure 10. Spectrograph No. 1, Minimum Resolution versus Virtual Acceptance Half-Angle

It should be remarked that the resolution capability of the instrument as conceived will be greater than the minimum value plotted in the figures whenever the solar wind conditions are such that $V_o < 700$ km/sec. For example, Table 7 gives the range in resolution corresponding to $V_o = 300$ to 700 km/sec for two values of mass/charge number and an object slit width of 0.004 inch.

TABLE 7

RESOLUTION

Data of Table 1 with magnetic intensity = 2120 gauss; magnet radius = 3.937 inch; object slit width = 0.004 inch.

α'	M/Z = 2	M/Z = 3
0.1^o	664	664
0.5^o	588 to 630	570 to 616
1.0^o	486 to 566	434 to 550
2.0^o	261 to 486	203 to 416
4.0^o	87 to 250	64 to 218
6.0^o	38 to 132	26 to 101

3.7 DEFINITION OF SENSITIVITY

Fundamentally, the instrument sensitivity is concerned with the number of ions of any given species which must pass through the entrance aperture (object slit) in order to produce a detectable image on the photographic plate. Scattering losses, aberrations, and photographic emulsion response are the factors which determine a sensitivity parameter.

For convenience, a sensitivity parameter, τ, will be defined as the time (seconds) required for ions of a given species to produce a line of specified degree of blackening on the emulsion. In the derivation of τ, let

S^* = number of ions of a given species per cm^2 required to blacken a specified degree

Φ = number of ions of a given species per cm^2 - sec. incident upon the line

then,

$$\tau = \frac{S^*}{\Phi} \tag{13}$$

For the present application, the ion currents will be extremely small; therefore, scattering losses, due primarily to space charge repulsion, can be neglected. The various intermediary slits will be considered open to the passage of the entire ion beam emanating from the entrance aperture. That is, 100 percent instrument transmission is assumed; also, acceptance angles are taken to be small. It follows that

$$\Phi = \frac{\Phi_o a_s}{a_i} \tag{14}$$

where

Φ_o = ion flux of a given species incident upon entrance aperture

a_s = area of entrance aperture

a_i = area of blackened line

It should be noted that the effect of the emulsion on the sensitivity parameter is expressed by S^* and the effect of the instrument is introduced by the factor a_s/a_i. The area a_i is derived as follows:

$$a_i = \underbrace{\frac{r_m A_\gamma}{2R}}_{\text{line width}} \times \underbrace{2r_m(v_o A_v + \beta A_\beta)}_{\text{line length}} \tag{15}$$

where R = resolution is given in Figs. 8, 9, and 10, and Table 7. Also, the axial acceptance half-angle, β, can be replaced by α since both are identical in the design concept of this instrument.

Equation 13 can now be expressed as

$$T = \frac{S^* r_m^2 A_\gamma}{\Phi_o a_s R} (v_o A_v + \alpha A_\beta) \tag{16}$$

Owen (Ref. 13) has studied in detail the response of Ilford Q_2 emulsion to the radiation of ionizing particles. He found that the sensitivity of Ilford Q_2 plates increases linearly with increasing ion energy, inversely with the square root of the ion mass, and is independent of ionic charge. Similar results have been observed by other investigators (Ref. 14) who examined RCA thin-film plates and Kodak-Pathe' SC5 emulsion in addition to the Ilford Q_2. As a note, the SC5 emulsion is a centrifuged film which has reportedly detected Fe^+ ions in quantities 0.2 to 0.05 of those barely detectable with Ilford Q_2, that is, with a sensitivity to ions estimated about 10x that of Q_2.

The S* that is used in this discussion is related to the reciprocal of the emulsion sensitivity and consequently S* should vary with the root of the mass and inversely to the energy. However, the product of mass/charge times ion energy entering the magnetic sector has been constrained to be a constant (k) in the design concept in order to avoid the necessity of changing magnets. Consequently,

$$S^* \rightarrow \left(\frac{M}{Z}\right)^{3/2} \Big/ kZ^{1/2} \tag{17}$$

Again, the apparent dependence of S* on ionic charge is not of physical significance but only comes about due to the imposed constraint.

Hintenberger (Ref. 15) has also investigated the blackening of Ilford Q_2 plates by ions of different masses and energy. For example, he reports that 1.25×10^6 ions per cm^2 of H_2^+ with an energy of 9 kV suffices to produce a line of clearly visible blackening. On the other hand, Woolston et al (Ref. 16) have found that Cs^+ ions of the same energy require an accumulation of $\approx 10^9$ ions per cm^2 to produce a line blackened to 50 percent saturation. After correcting this value by the ratio of the square roots of H_2-mass to Cs-mass, it is seen that 50 percent saturation blackening can be expected by approximately 10^8 ions per cm^2 of H_2^+, i.e. about 100 x the accumulation required to obtain a line just clearly visible. This overload feature of the spectrograph permits operation of the instrument without close monitoring of the exposure time.

Using the data given above, values of the instrument sensitivity parameter, τ, can be calculated for H_2 with regard to the following chosen conditions:

$$S^* = 1.25 \times 10^6 \quad \text{(line clearly visible)}$$

$$S^* = 10^8 \quad \text{(50 percent blackening)}$$

$$\text{Mass/charge} = 2 \; (H_2^+)$$

$$\text{Energy} = \frac{k}{\text{Mass/charge}} = \frac{22.5}{2} = 11.25 \text{ kV}$$

From Table 1; $A_\gamma = 0.6157$

$A_v = 1.64$

$A_\beta = 1.084$

From Figure 9; Mass/charge (2), α' (3^{o}) $\rightarrow$ R = 170

$$\text{Entrance aperture} = \begin{cases} 0.05 \text{ mm (width)} \\ 5.0 \text{ mm (length-arbitrary)} \end{cases}$$

$$\therefore \; a_s = 0.25 \text{ mm}^2$$

$$r_m = 100 \text{ mm}$$

From Figure 6; $\alpha' = 3^{o} \rightarrow \alpha = 1.71^{o} \rightarrow 0.0298$ radian

(note: the upper curve, V_o = 700 km/sec at a mass/charge = 2, is used since this corresponds to the calculation of R)

$$v_o = \frac{\text{entrance aperture length}}{2r_m} = 0.025$$

The resulting computation yields

$$\tau = \frac{10.6 \; S^*}{\Phi_o} \qquad (18)$$

TABLE 8

SENSITIVITY PARAMETER

Spectrograph No. 1 with $\alpha' = 3^{o}$; magnetic intensity = 2120 gauss; magnet radius = 100 mm (3.937 inch); object (entrance) aperture area = 0.25 mm^2; mass/charge = 2; resolution = 170.

Φ_o, $\text{cm}^{-2}\text{-sec}^{-1}$	Clearly Visible (sec.)	50 Percent Saturation (sec.)
10^4	1325	10^5
10^6	13.25	1000
10^8	0.13	10

Equation 18 renders Table 8 which lists exemplary values of the sensitivity parameter for the range of component flux intensity assumed to exist in the solar wind.

3.8 MISCELLANEOUS DETAILS

3.8.1 HIGH-VOLTAGE REQUIREMENTS

A direct current high voltage supply is required for several elements of the spectrograph design concept. Figure 11 shows the locations of the various points of high voltage. The magnitude of the requirement is demonstrated in Fig. 12, which indicates the dependence upon the virtual acceptance half-angle.

There is a precedence in the use of such high voltages in space instrumentation. C. Snyder (Ref. 17) is currently using an alternating supply of 12 kV in the OGO-5 experiment designed to measure plasma wind direction. On the one hand, the electronic specifications of a dc supply are less severe than those of a comparable ac supply. However, the voltages of the spectrograph must be highly regulated, at least to a degree equal to the reciprocal energy resolution (δ), i.e., less than 1%. It should be noted that the energy resolution is always greater than the mass/charge resolution, R. This can be shown as follows:

$$\text{ENERGY RESOLUTION} = \frac{U}{\Delta U} = \frac{1}{\delta} \equiv R_\delta$$

$$R_{\alpha \rightarrow 0} = \frac{0.5\, r_m A_\gamma}{S' A_u + 2 r_m \delta A_\delta} \equiv R(\max)$$

$$\delta_{\alpha \rightarrow 0} = \frac{S}{\ell} = \frac{\sqrt{2}\, S'}{\ell} \equiv \frac{1}{R_\delta(\max)}$$

Since, $r_m = \ell$ in Fig. 2, then

$$\delta_{\alpha \rightarrow 0} = \frac{\sqrt{2}\, S'}{r_m}$$

NOTES: UNLESS OTHERWISE SPECIFIED

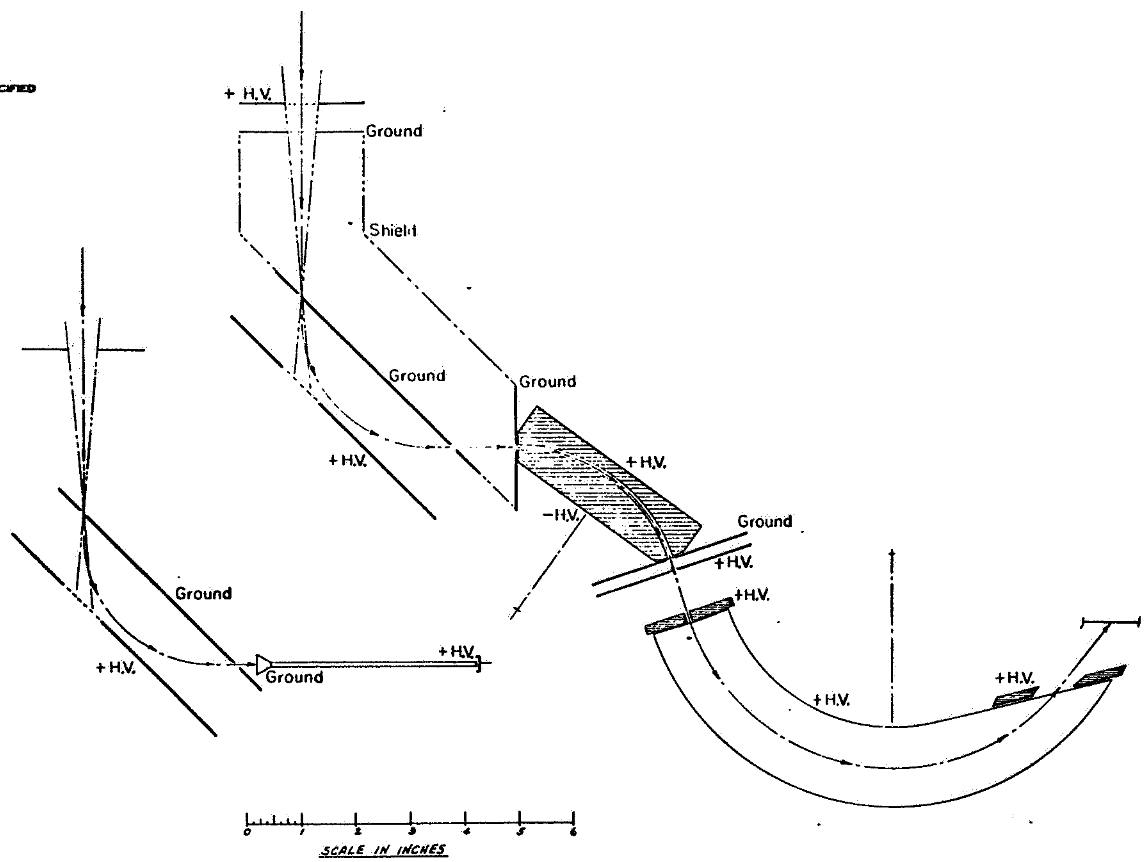

ELECTRO-OPTICAL SYSTEMS, INC.
A XEROX COMPANY
300 NORTH HALSTEAD STREET, PASADENA, CALIFORNIA 91107

TITLE DOUBLE-FOCUSING MASS/CHARGE SPECTROGRAPH HIGH VOLTAGE SCHEME

DRAWN B. L. Foreman

D 12705 3039-101

SCALE SHOWN SHEET 1 OF 1

3039-101

Figure 11.

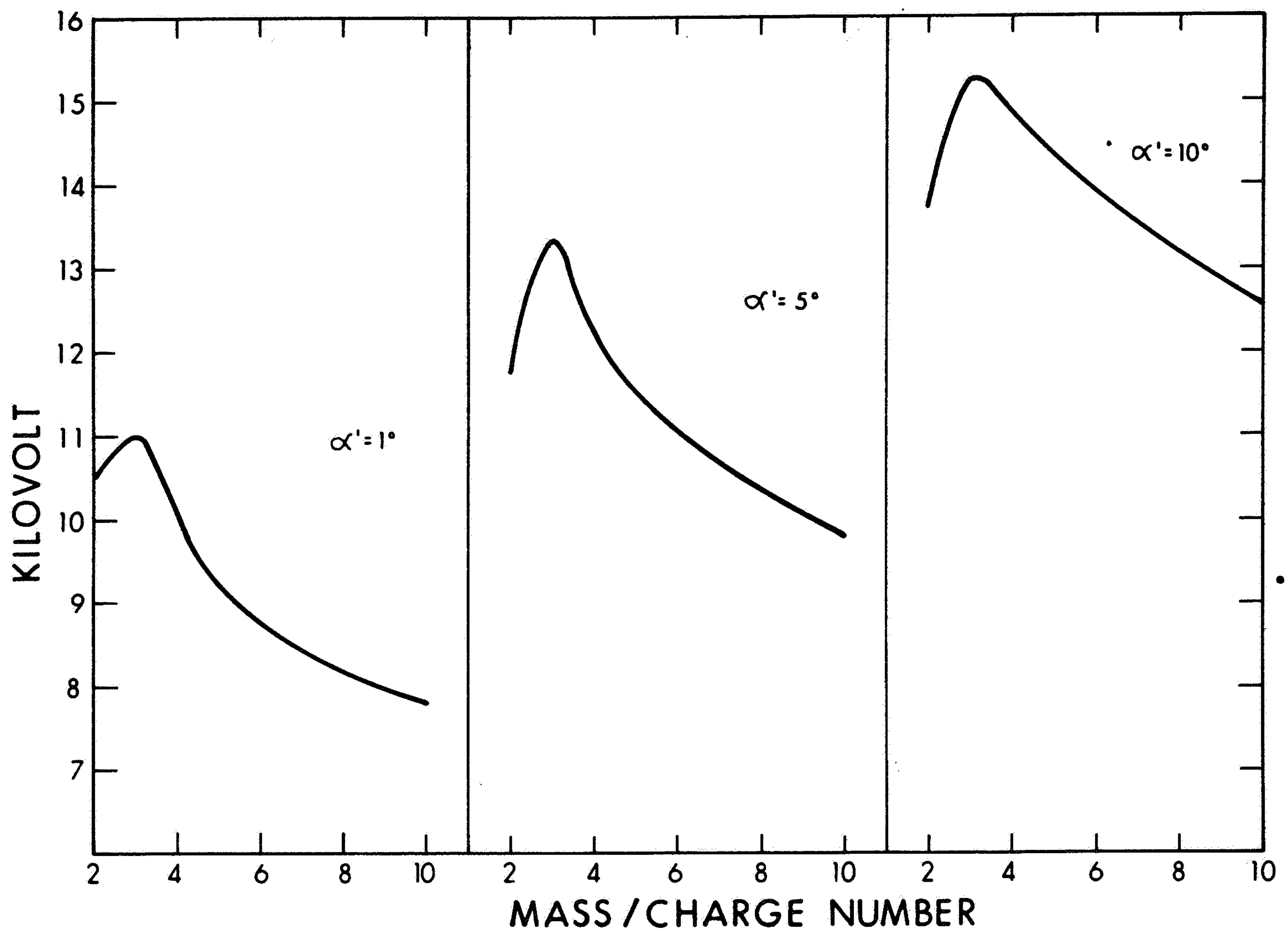

Figure 12. Indication of Dependence Upon Virtual Acceptance Half-Angle

or,

$$R(\max) = \frac{R_\delta(\max) \times A_\gamma}{\sqrt{2}(A_u + 2\sqrt{2}\,A_\delta)} = 0.63\ R_\delta(\max)$$

Therefore, in the last analysis, the electronics of the high voltage power supply might determine the resolution that can be realized apart from the physical limitations of the instrument.

3.8.1.1 Instrument Tuning

The instrument is tuned to a specific energy and mean mass/charge number $(M/Z)_o$ by adjusting the potentials across the various high voltage elements. Primarily, tuning is accomplished by varying the proton velocity tuner voltage V until this unit passes the energy of the maximum hydrogen ion flux as indicated by a peaking of the continuous channel electron multiplier (CCEM) output. The proton velocity corresponding to this energy is defined as V_o, the solar wind bulk velocity. A change in V_o can be detected by a change in the setting V required to peak the CCEM output. A variation in the amplitude of the peaked output which requires no adjustment of V would indicate a change in the proton ion density.

Using Equation 6, the proton velocity selector potential is determined by

$$V = \frac{0.584 \times 10^{-5}\ V_o^{\ 2}}{2} \quad \text{(kilovolt)}$$

where V_o is expressed in units of km/sec.

The remaining potentials involved in the instrument tuning are related to V as follows (refer to Table 6):

For a given mean value $(M/Z)_{oj}$,

$$\text{Accelerator voltage} = C_{j1}$$

$$\text{Filter voltage} = (M/Z)_{oj}V + C_{j2}$$

$$\text{Electric sector voltage} = \frac{2d\ (M/Z)_{oj}}{0.584\ r_e}\ V + C_{j3}$$

$$\text{Decelerator voltage} = \frac{(M/Z)_{oj}}{0.584}\ V + C_{j4}$$

where the C_{ji} are constants of different values (i) corresponding to the selected mean mass/charge number (j).

3.8.2 ELECTRIC SECTOR

In Fig. 3 the electric sector is identified as a spherical electrostatic analyzer. It is described by a parameter c (=1), Table 1, where c is defined as

$$c = \frac{\text{radius of the central path in the electric field}}{\text{axial radius of curvature (middle equipotential surface)}}$$

The dimension $r_m L_e$ (Fig. 2), locates the object slit at the radial focal plane of the sector such that the beam exiting the sector will be parallel (collimated) in the radial sense. In order that the beam will be completely collimated, that is in both radial and axial senses, the object slit must also be located at the axial focal plane. One of the reasons for choosing the data of Table 1 is that the radial and axial focal planes almost coincide for the spherical geometry. The axial focal length is given by the following expression:

$$\text{axial focal length} = \frac{r_m \cot(\sqrt{c}\,\phi_e)}{\sqrt{c}}$$

Theoretically, the two focal planes can be made to exactly coincide if $c = 1.062$, which means that the electric sector should actually be very slightly toroidal. Fringe fields are taken into account in the calculation of the radial focal length and are not involved in the calculation of the axial focal length. However, in practice the effect of the fringe field shields might alter the theoretical value of radial focal length somewhat.

The potential across the plates of the electric sector is directly proportional to their separation which, in turn, depends upon the real acceptance half-angles, α and β. Figure 13 shows the separation versus α for the data in Tables 1 and 2. The cases of Tables 3 and 4 would generate curves which would lie between those in Fig. 13.

3.8.3 MAGNETIC SECTOR

Again referring to Fig. 3, the magnetic sector is a permanent magnet with conical pole faces (Refs. 4, 18, 19). It produces a field which varies according to

$$B = B_o \left[\frac{r_m}{r}\right]^n$$

where B_o is the magnitude of the field at the position of the central path, r_m is the radius of the central path, and r is any radial position. The exponent, n, is called the inhomogeneity parameter. A choice of n slightly less than unity will result in an increase in resolving power over that which can be realized for the case of a homogeneous field, i.e., $n = 0$. Magnets with $n = 0.91$ have been built by Alekseevski et al (Ref. 20).

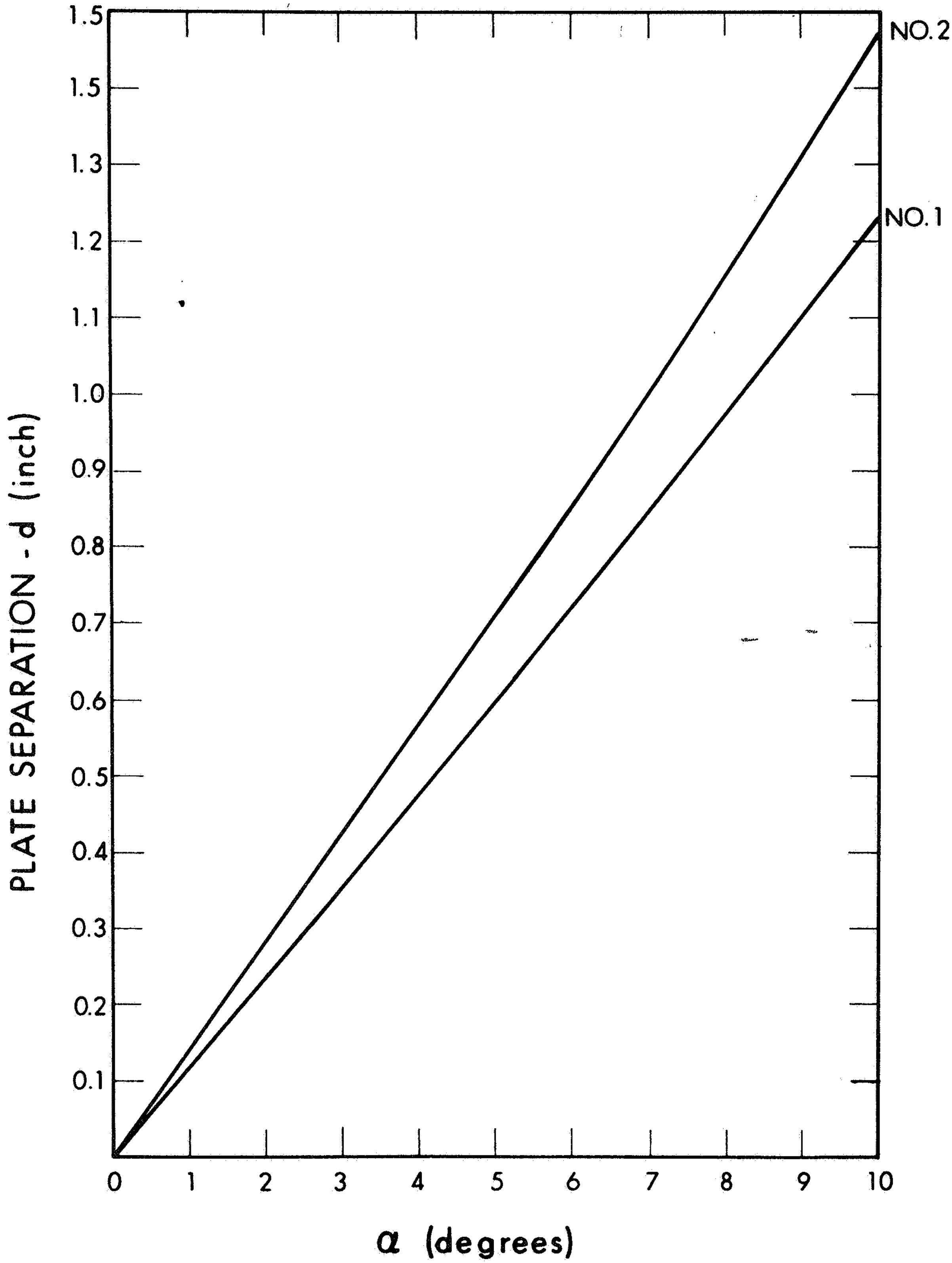

Figure 13. Separation versus α for Data in Tables 1 and 2

The dimension, $r_m L_m$ (Fig. 2), locates the image at the radial focal plane of the magnetic sector since the beam entering the magnet is collimated. Unlike the radial focal length, the axial focal length of the magnetic sector is affected by the magnetic fringe fields. When this effect is taken into account, the axial focal length turns out to be

$$\text{axial focal length} = 0.826 \text{ inch}$$

when the data of Table 1 are used. This means that the axial focal length is nearly one-half the radial focal length; so, perfect axial focusing at the image is not achieved theoretically. This is why the axial magnification $A_v = 1.64$ (see Section 3.7) at the image plane is greater than unity.

3.8.4 PHOTOGRAPHIC DETECTOR

As presently conceived, the photographic detector would consist of a magazine which would permit segments of photographic plate to be exposed selectively. Each segment would be approximately one inch, so the dispersion of mass/charge numbers would be limited to this extent. For example, the dispersion is given by

$$\text{dispersion} = 0.01 r_m A_\gamma$$

which is a measure of the spatial separation of two mass/charge numbers differing by one percent. Using the given values of r_m and A_γ, the dispersion would be 0.025-inch. This means that a segment of plate one inch in length in the radial plane would be more than sufficiently wide to accept a spread of ±20 percent in mass/charge numbers.

3.8.4.1 Cosmic Radiation

The use of photographic materials in space naturally raises the question concerning the effects of cosmic radiation. In the present application, however, the photographic plates are only about one micron in thickness. Considering the extremely high energies of the typical cosmic ray particle and the correspondingly long mean free path, it can be shown that no significant interaction with the photographic emulsion will result within the period of time that the plates would be exposed to this type of radiation.

3.8.5 DIMENSIONS

Figure 3 shows the dimensions of the instrument. It has been designed in concept so that the accelerator/collimator unit can be easily inserted into a six-inch port in order to intercept the solar wind ion beam. To further conserve space, an effect of the energy filter is to bend the ion beam through the angle of 90°. The dimensions shown in Fig. 3, however, do not necessarily include the electronic package.

3.8.6 LIGHT FLUX REJECTION

The problem of light flux rejection has been encountered in space experiments which use detectors that channel the solar light radiation, along with the ion beam, to the sensing element. The electrostatic analyzer is an example of such a detector. Ogilvie et al (Ref. 21) have constructed a portion of their electrostatic analyzer with tungsten mesh, thus forming a light trap which seemingly has been effective in preventing channeling.

Channeling in the electric sector of a double-focusing instrument is not so severe when there is no sensing element at the exit terminal of the electric sector. The tortuous path which an ion beam must follow results in light rejection being an inherent feature of this instrument. However, to further enhance light rejection a trap similar to that of the Ogilvie design is provided in the energy filter and the proton velocity tuner shown as a screen in Fig. 3. These units bend the ion beam 90° out of the path of the light flux such that the spherical electrostatic analyzer does not see this unwanted radiation.

SECTION 4

CONCLUSION

The results of the feasibility study of an astronaut-operated double-focusing mass/charge spectrograph design concept suitable for use in an Apollo Command Module have been presented in detail in Sections 2 and 3. These results are summarized as follows:

The instrument is capable of a resolution in the range 100 to 200 for mass/charge numbers in the range 2 to 4 and an acceptance cone half-angle of three degrees. Data are presented which relate resolution to mass/charge number and acceptance half-angle. The resolution is found to increase rapidly as the acceptance angle is decreased.

Mass/charge in the range 2 to 10 can be accepted by the instrument using one permanent magnet. This is accomplished by using an accelerator unit and a decelerator unit which together provide the method of selecting a given mass/charge number.

A velocity deviation of ±0.20 can be accepted by the instrument. However, only a deviation of ±0.10 is necessary in order to display a mass/charge deviation of ±0.20 over a one inch segment of photographic plate.

Sensitivity has been defined as the time required for ions of a given species to produce a line of specified degree of blackening on the photographic emulsion and a sensitivity parameter has been analytically derived. The sensitivity parameter is inversely proportional to the resolution. A sample calculation shows that an ion species of flux intensity 10^4 per cm^2-sec could be detected with a resolution of 170 on Ilford Q_2 emulsion after approximately twenty minutes exposure.

Light flux rejection can be adequately achieved by features of the instrument design.

Dimensions and weight of the instrument are not considered to be critical. A high voltage supply of approximately twelve kilovolts would be required with at least one percent regulation or better. Mass/charge and solar wind velocity tuning would be accomplished by interdependently varying the potentials across several high voltage elements of the instrument.

SECTION 5

REFERENCES

1. H. Wollnik, Nucl. Instr. and Meth. 52, 250-272 (1967)
2. H. Wollnik, Nucl. Instr. and Meth. 34, 213-221 (1965)
3. H. Wollnik, Nucl. Instr. and Meth. 59, 277-282 (1968)
4. H. Wollnik, Nucl. Instr. and Meth. 53, 197-215 (1967)
5. H. Wollnik, Nucl. Instr. and Meth. 36, 93-104 (1965)
6. G. A. Harrower, Rev. Sci. Instr. 26, 850 (1955)
7. A. J. Hundhausen, J. R. Asbridge, S. J. Bame, H. E. Gilbert, and I. B. Strong, J. Geophys. Res. 72, 87 (1967)
8. M. Neugebauer and C. W. Snyder, in The Solar Wind, edited by R. J. Mackin and M. Neugebauer (Pergamon Press, New York, 1966) p. 3.
9. S. J. Bame, A. J. Hundhausen, J. R. Asbridge, and I. B. Strong, Phys. Rev. Letters 20, 393 (1968)
10. Proceedings of the Plasma Space Science Symposium, 11 to 14 June (1963), Astrophysics and Space Science Library, edited by C. C. Chang and S. S. Huang, vol. 3 (D. Reidel Publishing Co., Dordrecht, Holland, 1965), p. 68.
11. (private communication)
12. R. Ludwig, Z. Naturforschg. 22a, 553 (1967)
13. E. B. Owens, App. Spectroscopy 16, 148 (1962)
14. R. E. Honig, J. R. Woolston, and D. A. Kramer, Rev. Sci. Instr. 38, 1703 (1967).
15. H. Hintenberger, Ann. Rev. Nucl. Sci. 12, 441 (1962)
16. J. R. Woolston, R. E. Honig, and E. M. Botnick, Rev. Sci. Instr. 38, 1708 (1967)
17. (private communication)
18. H. Fabricius, Nucl. Instr. and Meth. 61, 251 (1968)
19. H. A. Tasman, Advances in Mass Spectrometry, vol. 1 (Pergamon Press, New York, 1959) p. 36.
20. N. E. Alekseevski, Dokl. Akad. Nauk SSSR 100, 229 (1953)
21. K. W. Ogilvie, N. McIlwraith, and T. D. Wilkerson, Rev. Sci. Instr. 39, 441 (1968)